Opto-Electronic Science

Supplementary information

xxxx 2025, Vol. x, No. x

DOI: 10.29026/oes.2025.240036 CSTR: 32246.14.oes.2025.240036

Operando monitoring of state of health for lithium battery via fiber optic ultrasound imaging system

Geng Chen[1], Anqi Wang[1], Yi Zhang[2], Fujun Zhang[1], Dongchen Xu[1], Yueqi Liu[1], Zhi Zhang[1], Zhijun Yan[1,3], Zhen Li[2], Hao Li[1]* and Qizhen Sun[1,3]*

[1]School of Optical and Electronic Information, Huazhong University of Science and Technology, Wuhan 430074, China; [2]State Key Laboratory of Material Processing and Die & Mould Technology, School of Materials Science and Engineering, Huazhong University of Science and Technology, Wuhan 430074, China; [3]Hust-Wuxi Research Institute, Huazhong University of Science and Technology, Wuxi 214174, China.

*Correspondence: H Li, E-mail: lhbeyond@hust.edu.cn; QZ Sun, E-mail: qzsun@mail.hust.edu.cn

This file includes:

Supplementary information for this paper is available at https://doi.org/10.29026/oes.2025.240036

Section 1: The experiment setup of the sensitivity calibration for the fiber optic ultrasound sensor

In Fig. S1(a) and S1(b), the PZT is placed 30 mm against the ultrasound sensor and the PVDF hydrophone for calibration. When the output voltage of the signal generator is 1 V, the output signal of the PVDF hydrophone is depicted in Fig. S1(c), with the signal amplitude of around 0.477 mV. Hence, the input ultrasound pressure can be calculated by Eq. (S1).

$$P = \frac{V_{\mathrm{PP}}}{S_{\mathrm{h}}} , \tag{S1}$$

where S_{h}=17.2 mV/kPa is the sensitivity of the PVDF hydrophone when the ultrasound frequency is 500 kHz. Therefore, the input pressure is calculated to be 27.73 Pa when the output voltage of the signal generator is 1 V.

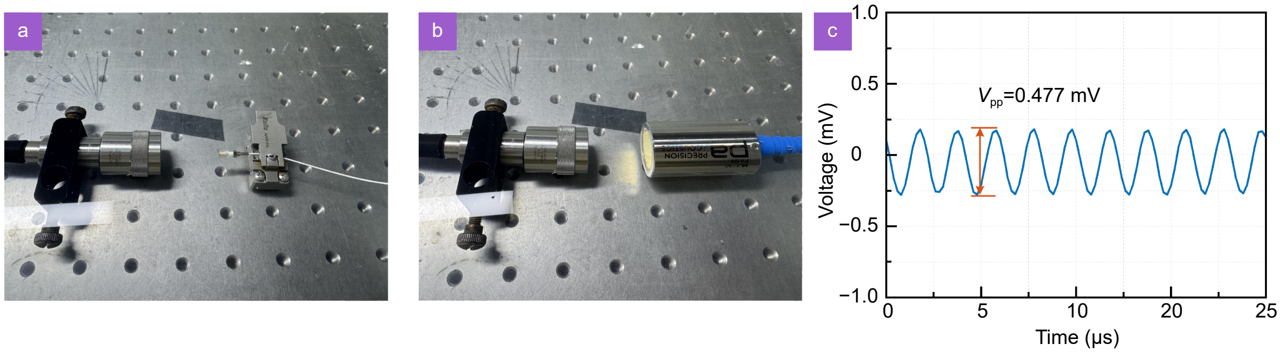

Fig. S1 | (**a**) The relative position of the PZT and the fiber optic ultrasound sensor. (**b**) The relative position of the PZT and the PVDF hydrophone. (**c**) The output signal of the PVDF hydrophone when the voltage frequency is 500 kHz.

Section 2: The stability of the sensor in detecting ultrasound signals

To test the stability of the sensor during the scanning process, we carried out the experiment to detect the ultrasound signal every 10 s in nearly 6 h, and the signal and ToF is quite stable in Fig. S2(a). The signal intensity is further analyzed in Fig. S2(b), where the intensity fluctuation is about 12%, which is negligible compared to the signal attenuation caused by the batteries.

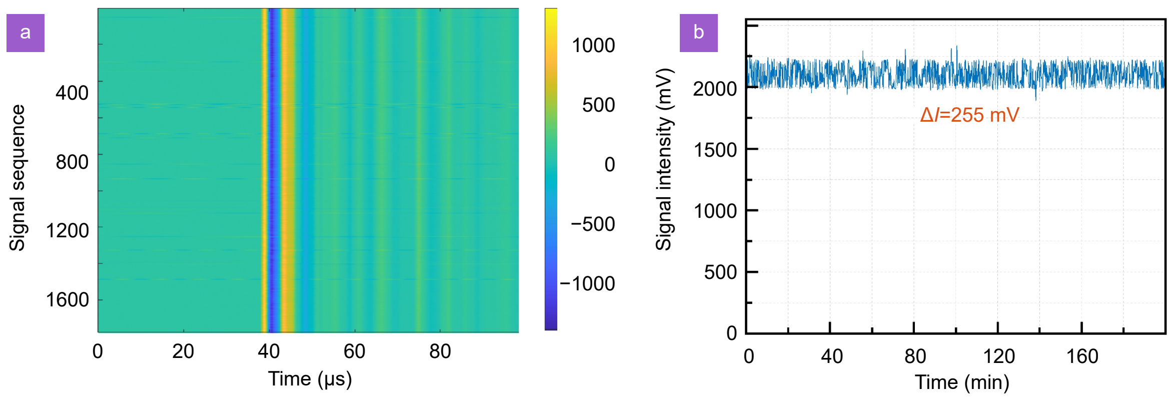

Fig. S2 | (**a**) The signals during the scanning process. (**b**) The signal intensity during the scanning process.

Section 3: The imaging result of a lithium-ion ferrous phosphate/graphite (LFP||Gr) battery

To verify the ability of the imaging system in BHM, a LFP||Gr battery is imaged via this fiber optic ultrasound imaging system, and the result is described in Fig. S3(c), where we can see that the electrodes have been clearly imaged. The edge of the battery is almost blue, indicating a low transmission of ultrasound. While the inner part of the battery shows a higher signal compared to signal of the edge, which means the battery is still chargeable and not fault.

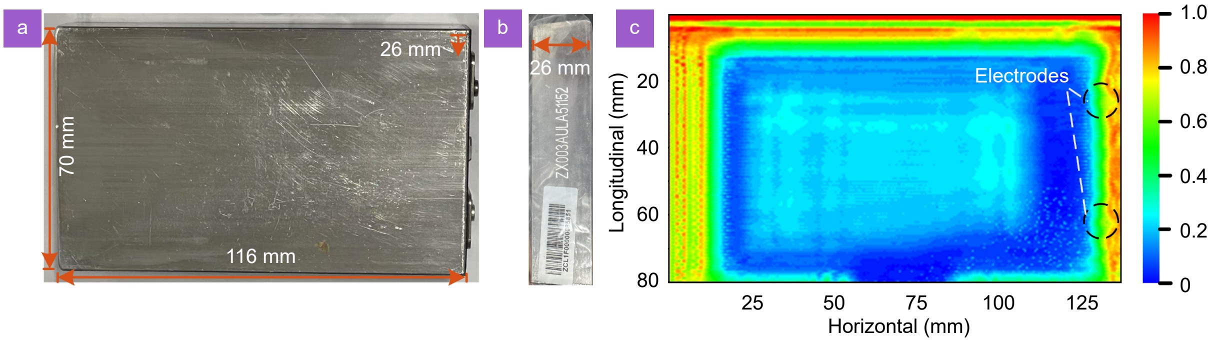

Fig. S3 | (**a**) The front view of the LFP||Gr battery. (**b**) The side view of the LFP||Gr battery. (**c**) The imaging result of the LFP||Gr battery.

Section 4: The imaging results of the AFLMB during the formation process

In Fig. S6(b) and Fig. S6(c), the battery part and gas part are clearly separated, respectively. Then, the gas ratio is acquired by dividing the number of elements in Fig. S6(c) by the number of elements in Fig. S6(b).

Applying the above method to the images in Fig. S4 and Fig. S5, the gas ratio variation during the formation process can be plotted and analyzed.

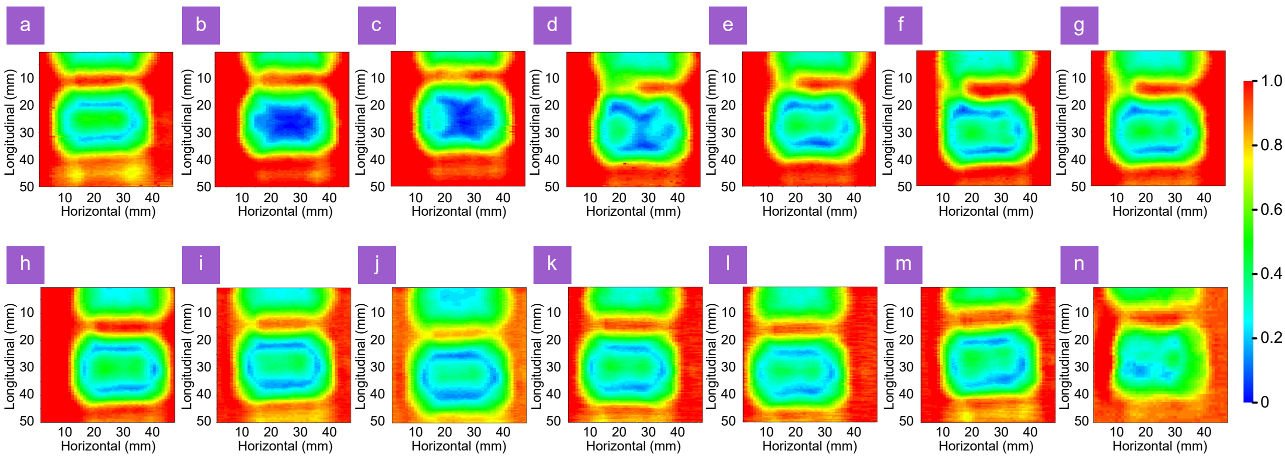

Fig. S4 | The ultrasound image of the AFLMB after charging for (**a**) 0 h, (**b**) 1 h, (**c**) 2 h, (**d**) 3 h, (**e**) 4 h, (**f**) 5 h, (**g**) 6 h, (**h**) 7 h, (**i**) 8 h, (**j**) 9 h, (**k**) 10 h, (**l**) 11 h, (**m**) 12 h, (**n**) 13 h.

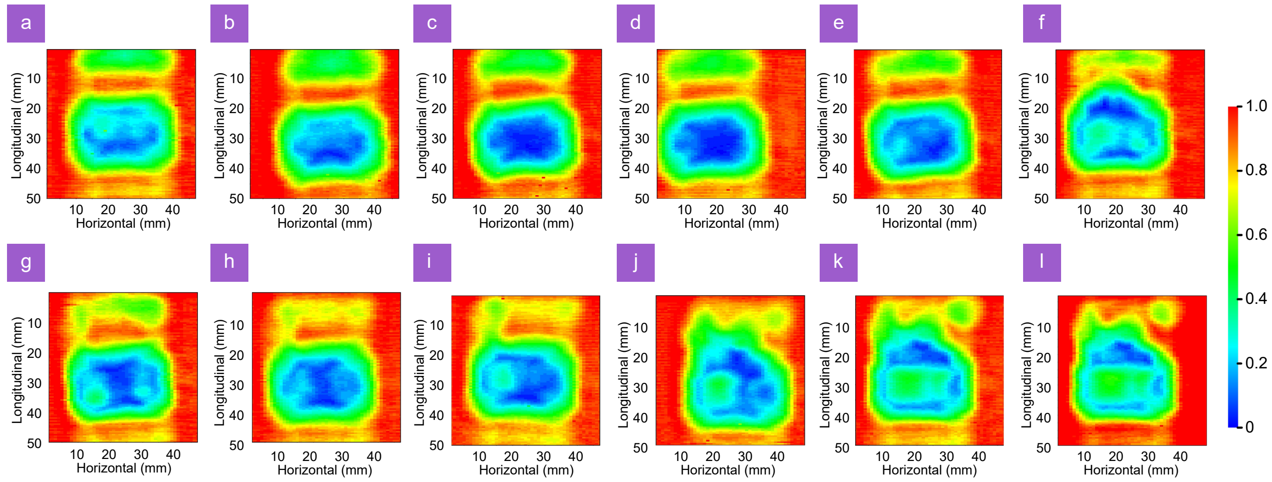

Fig. S5 | The ultrasound image of the AFLMB after discharging for (**a**) 1h, (**b**) 2h, (**c**) 3h, (**d**) 4h, (**e**) 5h, (**f**) 6h, (**g**) 7h, (**h**) 8h, (**i**) 9h, (**j**) 10h, (**k**) 11h, (**l**) empty.

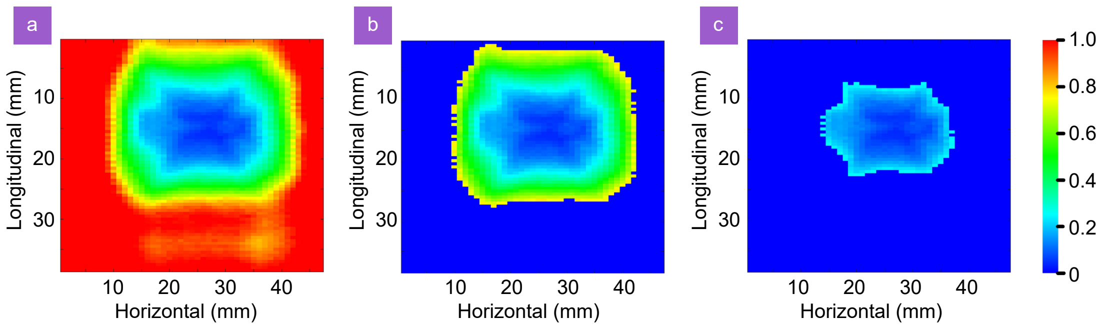

Fig. S6 | (**a**) The original ultrasound image of an AFLMB. (**b**) The battery part of the original ultrasound image. (**c**) The gas part of the original ultrasound image.

Section 5: The performance of conventional piezoelectric transducer with this fiber optic ultrasound sensor

The NEP of different piezoelectric transducers are listed in Table S1, where the minimum NEP of them is around several pascal, demonstrating a poorer performance compared with our work. The low NEP of around 63.5 mPa enables the system to detect ultrasound signals with pretty low noise.

Table S1 | The NEP compared with conventional piezoelectric transducers.

	CMUT[S1, S2]	PMUT[S3]	PVDF[S4–S6]	Piezoelectric TUT[S7, S8]	Piezopolymer detector[S9]	This work
NEP	0.085–0.23 mPa/Hz$^{1/2}$; 30.7 mPa/Hz$^{1/2}$	77 Pa, 86 Pa, 156 Pa	1.6 Pa; 14 Pa; 5.6 mPa/Hz$^{1/2}$	530 Pa; 15.7 Pa, 11.9 Pa, 9.6 Pa	0.3 Pa, 1.2 Pa	63.5 mPa

The NEP expressed in Pa and Pa/Hz$^{1/2}$ can be described in Eq. (S2).

$$NEP_{\mathrm{Pa}} = NEP_{\mathrm{Pa}/\sqrt{\mathrm{Hz}}} \cdot \sqrt{B}\ , \tag{S2}$$

where B is the bandwidth of the sensor, which is 218 kHz in Fig. 2(e). Hence, the NEP of the sensor can be calculated as 13.6 μPa/Hz$^{1/2}$. The result is quite smaller than the traditional piezoelectric transducer, indicating a great performance of the sensor in detecting ultrasound waves.

References

S1. Zangabad RP, Lee H, Zhang XT et al. A high sensitivity CMUT-based passive cavitation detector for monitoring microbubble dynamics during focused ultrasound interventions. *IEEE Trans Ultrason Ferroelectr Freq Control* **71**, 1087–1096 (2024).

S2. Dew EB, Kashani Ilkhechi A, Maadi M et al. Outperforming piezoelectric ultrasonics with high-reliability single-membrane CMUT array elements. *IEEE Trans Ultrason Ferroelectr Freq Control* **8**, 59 (2022).

S3. Ledesma E, Uranga A, Barniol N. A single-chip AlScN PMUTs-on-CMOS hydrophone. *IEEE Sens J* **24**, 21311–21320 (2024).

S4. van Neer PLM, Peters LCJM, Verbeek RGFA et al. Flexible large-area ultrasound arrays for medical applications made using embossed polymer structures. *Nat Commun* **15**, 2802 (2024).

S5. Liu YH, Kurnikov A, Li WY et al. Highly sensitive miniature needle PVDF-TrFE ultrasound sensor for optoacoustic microscopy. *Adv Photonics Nexus* **2**, 056006 (2023).

S6. Hass K, Insabella RM, González MG et al. A method for the calibration of wideband ultrasonic sensors for optoacoustics. *Rev Sci Instrum* **92**, 064904 (2021).

S7. Qiu CR, Zhang ZQ, Xu ZQ et al. Transparent ultrasonic transducers based on relaxor ferroelectric crystals for advanced photoacoustic imaging. *Nat Commun* **15**, 10580 (2024).

S8. Mirg S, Chen HY, Khandare S et al. Noise considerations in piezoelectric transparent ultrasound transducers for photoacoustic imaging applications. *Proc SPIE* **11960**, 119600S (2022).

S9. Kurnikov A, Sanin A, Ben XLD et al. Ultrawideband sub-pascal sensitivity piezopolymer detectors. *Ultrasonics* **141**, 107349 (2024).